Hierarchical porous ϵ-MnO2 from perovskite precursor: Application to the formaldehyde total oxidation

Yin Xu, Jérémy Dhainaut, Guillaume Rochard, Jean-Philippe Dacquin, Anne-Sophie Mamede, Jean-Marc Giraudon, Jean-François Lamonier, Hui Zhang, Sébastien Royer

Contents lists available at ScienceDirect

Chemical Engineering Journal

journal homepage: http://ees.elsevier.com

Hierarchical porous ε-MnO_2 from perovskite precursor: Application to the formaldehyde total oxidation

Yin Xu [a,b], Jérémy Dhainaut [b,c], Guillaume Rochard [b], Jean-Philippe Dacquin [b], Anne-Sophie Mamede [c], Jean-Marc Giraudon [b], Jean-François Lamonier [b], Hui Zhang [a,*], Sébastien Royer [b,*]

[a] Department of Environmental Science and Engineering, Hubei Environmental Remediation Material Engineering Technology Research Center, Wuhan University, Wuhan 430079, China
[b] Univ. Lille, CNRS, ENSCL, Centrale Lille, Univ. Artois, UMR 8181-UCCS-Unité de Catalyse et de Chimie du Solide, F-59000 Lille, France
[c] Univ. Lille, CNRS, INRA, Centrale Lille, ENSCL, Univ. Artois, FR 2638 – IMEC – Institut Michel-Eugène Chevreul, F-59000 Lille, France

ARTICLE INFO

Keywords
Hierarchical ε-MnO_2
Perovskite acid treatment
Pseudomorphic process
Heterogeneous catalysis
Formaldehyde oxidation

ABSTRACT

A simple template-free method, based on a mineral acid etching process using manganite perovskite ($LaMnO_3$) as precursor, was successfully developed to obtain a series of 3D meso/macro-porous materials. The $LaMnO_3$ transformation was fully investigated using ICP, XRD, N_2 physisorption, TPR, TPD, SEM, TEM/EDS and XPS. This transformation proceeds through a soft-chemical process involving the dissolution of trivalent lanthanum and manganese from the perovskite structure and the dismutation of Mn^{3+} cations into MnO_2 and Mn^{2+} species. Strength and oxidizing properties of the acid used as modifying agent strongly impact textural and redox surface properties of the resulting materials. Specifically, extending the acid etching duration promotes the surface area and pore volume of the materials while developing interconnected macro-mesoporous networks. In our case, this soft process allowed us to obtain the ε-MnO_2 phase with hierarchical porosity without any template. Superior catalytic properties of ε-MnO_2 were observed toward HCHO oxidation as well as a good catalytic stability with respect to other macro-mesoporous counterparts. In the light of the experimental results, such performances can be related to the formation of a meso/macro-porous structure conferring high surface area and good accessibility of the active surface sites. The latter exhibit greater redox ability of the manganese species and a higher density of active surface oxygen species with respect to the perovskite precursor.

1. Introduction

Formaldehyde (HCHO) is one of the major indoor air pollutants, mainly emitting from various building materials and household products such as paints, textiles, adhesives, pressed-wood products (plywood, fiber board and particle board) and other decorating materials [1]. The exposure to HCHO could threaten human health and cause symptoms such as edema, eye and skin irritation, headaches, and nasal tumors [1,2]. As a consequence, HCHO has been regarded as carcinogenic for humans (Group 1) by the International Agency for Research on Cancer (IARC) since 2004 [3].

Various approaches have been proposed to remove formaldehyde in the air, such as plasma technology [4], adsorption [5,6], heterogeneous catalysis oxidation including photocatalysis [7–9] and thermal oxidation [10,11]. Among the most efficient approaches is heterogeneous catalytic oxidation, as it is not limited to an adsorption capacity, and it does not require any large equipment such as a generator of light or plasma. Low temperature – ideally room temperature – catalytic oxidation has been deemed as a promising strategy for the elimination of indoor HCHO owing to its mild control conditions and low energy demand.

Among various classes of catalysts, noble metal-based catalysts (e.g., Pt, Au, Rh, and Pd) are extensively used for air pollutants remediation [12,13], especially as they were reported to oxidize VOCs (e.g., HCHO) totally at relatively low temperatures. For instance, HCHO is efficiently converted into CO_2 at room temperature over supported noble metals [13,14]. Nevertheless, their current application will be restricted owing to their high cost and the needs to reduce the amount of critical materials of strategic importance such as the Platinum Group Metals (PGM). However, converting HCHO at low temperature remains challenging with noble metal-free catalysts. Most efficient catalysts reported are pure and doped manganese (IV) oxides [13]. In this case, HCHO conversion (when calculated from CO_2 production) generally occurs at temperatures above 150 °C for pure manganese oxide [10,15]. However, even if conversion occurs only above 100 °C, abatement of formaldehyde can be achieved at ambient temperature, due to the adsorption/saturation of the material surface. Therefore, the search for low-cost and efficient catalysts based on readily available elements

* Corresponding authors.
E-mail addresses: eeng@whu.edu.cn (H. Zhang); sebastien.royer@univ-lille.fr (S. Royer)

https://doi.org/10.1016/j.cej.2020.124146
Received 2 October 2019; Received in revised form 24 December 2019; Accepted 15 January 2020
Available online xxx
1385-8947/

has brought supported or unsupported transition metal oxides to the forefront for environmental clean air applications (oxidation of volatile organic compounds and toxic hydrocarbons, catalytic decomposition/reduction of NO_x) [9,13]. Among the available metal oxides, the rich chemistry of manganese oxide promotes various polymorphs (β-MnO_2, γ-MnO_2, α-Mn_2O_3, γ-Mn_2O_3, α-Mn_3O_4, and Mn_5O_8…) wherein manganese elements can be found with various oxidation states (+II, +III, +IV). Moreover, low volatility and low toxicity of manganese oxide make it promising as a viable noble-metal free catalytic system. In order to reduce the performance gap between noble metals and transition metal oxides, the research of strategies allowing the enhancement of metal support interactions [16] and/or the improvement of textural properties (surface area, pore shape/size/orientation) is needed. In most of the studies, enhanced textural properties usually request soft/hard templating technologies involving more delicate protocols which are usually assigned to the template infiltration and removal processes [17]. To our knowledge, ε-MnO_2 phase with hierarchical porosity was only obtained by electrodeposition of nanostructured manganese oxides on bubble-covered Ni foam used as host support [18]. In consequence, ε-MnO_2 solids were rarely reported for catalysis [19,20]. In our work, we took advantage of the acid etching process developed earlier [21–23] by using perovskite as ε-MnO_2 precursor. Acid etching is a soft chemical method commonly used to modify the structure of materials [24–27], improving their catalytic activity [21–23,28–31] or some functions like their conductivity [32]. For instance, an acidic treatment was reported to preferentially dissolve silver from a silver-gold alloy, leaving behind pure gold with a higher surface area [24]. Kudo et al. [25] and Sugimoto et al. [27] have reported the conversion of an Aurivillius phase, $Bi_2W_2O_9$ and $Bi_2O_2[SrNaNb_3O_{10}]$, into $H_2W_2O_7$ and $H_{1.8}[Bi_{0.21}Sr_{0.80}Na_{0.95}Nb_3O_{10}]$ respectively by hydrochloric acid treatment. Selective dealumination was also reported when etching a microporous aluminosilicate H-Y (FAU) zeolite with hydrochloric acid, leading to the formation of a micro/meso-porous USY zeolite with improved stability and catalytic activity [33]. Herein, we propose the first application of a hierarchical ε-MnO_2 catalyst for HCHO oxidation at low temperature. By adjusting acid etching conditions, a facile one-step approach was developed to form in situ a series of high surface area perovskites with A-site (La) deficiency, MnO_2/perovskite and pure ε-MnO_2 materials with hierarchical porosity. Based on extensive characterizations, emphasis was made on the understanding of the LMO perovskite conversion mechanism toward ε-MnO_2.

2. Experimental

2.1. Synthesis of $LaMnO_{3.15}$ catalyst

$LaMnO_{3.15}$ was prepared following a conventional citric acid complexation method starting from the metal nitrate precursors $Mn(NO_3)_2{\cdot}xH_2O$ (98.0%, Aldrich) and $La(NO_3)_3{\cdot}6H_2O$ (≥99.0%, Sigma-Aldrich), and citric acid (+99.5%, Alfa Aesar).

For the synthesis, a molar ratio $(n_{Mn} + n_{La})/n_{citric\ acid}$ of 1 was applied. Typically, 3.7 g of manganese nitrate and 7.0 g lanthanum nitrate were dissolved in 40 mL of distilled water. In a second beaker 6.9 g of citric acid were dissolved in 40 mL of distilled water, and the resulting clear solution was added drop-wise to the solution containing the metal precursors under magnetic stirring. The resulting homogeneous solution was stirred for 1 h at 40 °C, and overnight at room temperature. A rotary evaporation step was used to remove the excess of water, resulting in a gel. The obtained gel was thermally treated in a muffle oven under air over two steps: 180 °C for 1 h (3 °C/min), and 700 °C for 8 h (2 °C/min).

2.2. Synthesis of non-stoichiometric LMO and ε-MnO_2 catalysts by acid etching process

By adjusting properly acid etching conditions, a facile approach was developed to form in situ a series of non-stoichiometric perovskites [34–36], MnO_2/perovskite composites and pure ε-MnO_2 phase with high surface area. Typically, 1.0 g of $LaMnO_{3.15}$ (LMO) was added to 250 mL of a 3 M nitric acid (65 ~ 70%, Alfa Aesar) solution and stirred at 200 rpm. At selected time intervals of 10 min, 60 min, 180 min, 240 min, 360 min, 14 h, and 22 h, the solid was filtered on a 0.2 μm PTFE membrane filter (Whatman™), washed with deionized water and dried in the oven at 60 °C for 24 h. The as-obtained samples were labeled as LM-10, LM-60, LM-180, LM-240, LM-360, LM-14h and LM-22h, respectively.

2.3. Catalytic oxidation of formaldehyde (HCHO)

The catalytic oxidation of formaldehyde (HCHO) was carried out in a fixed bed reactor (internal diameter = 8 mm), loaded with 0.20 g of the catalyst. Catalyst activation was performed in situ at 300 °C for 1 h under 20 vol% O_2/He, with a flow rate of 100 mL·min^{-1}. Gaseous formaldehyde was produced from paraformaldehyde in a permeation tube placed in a permeation chamber (Dynacalibrator, VICI Metronics, Inc.), which was kept at a constant temperature of 100 °C. The reacting gas containing 100 ppm of HCHO mixed with the 20 vol% O_2/He mixture was stabilized at 300 °C for another 1 h. Afterwards, the reacting gas was sent toward the fixed bed reactor and its temperature was controlled following a decreasing rate of 0.5 °C/min from 300 °C to 100 °C, at a rate of 0.2 °C/min in the range of 100 ~ 25 °C. The total flow rate was 100 mL/min, corresponding to a gas hourly space velocity (GHSV) of 30 L g_{cat}^{-1} h^{-1}. The effluent gas was monitored online by a gas chromatograph (GC, Varian) equipped with a thermal conductivity detector. Separations were performed using two columns: one CP-Sil 5 CB column channel (8 m) for HCHO analysis, and one COX column channel (1 m) for CO_2 analysis.

The formaldehyde (HCHO) oxidation into CO_2 was expressed as HCHO conversion, while HCHO elimination refers to the removal efficiency of HCHO from the gas flow. They were calculated using the following equations, respectively:

$$\text{HCHO conversion (into CO2)} = \frac{[CO_2]_t}{[HCHO]_0} \times 100\% \quad (1)$$

$$\text{HCHO elimination} = \frac{[HCHO]_0 - [HCHO]_t}{[HCHO]_0} \times 100\% \quad (2)$$

where $[HCHO]_t$ and $[CO_2]_t$ are assigned to the concentration at time t as monitored by GC, and $[HCHO]_0$ is the initial HCHO concentration (100 ppm).

During the stability test, a fresh catalyst was first activated as indicated before (300 °C, 1 h under 20 vol% O_2/He, 100 mL/min). Then the reacting gas (100 ppm HCHO in 20 vol% O_2/He, 100 mL/min) was passed through the catalyst bed at 99 °C (based on LM-22h T50 results) for at least 55 h.

2.4. Characterization

X-ray diffraction patterns (XRD) were collected on a Bruker D8 Advanced AXS diffractometer equipped with Cu $K_{\alpha1}$ monochromatic radiation source (λ = 1.5418 Å) and operated at 40 kV and 30 mA. X-ray diagrams were recorded within the 10°–80° region with a 0.02° step size (step time = 1 s). N_2-physisorption isotherms were recorded at −196 °C on a gas sorption system Tristar II Plus from Micromeritics. Before analysis, the samples were outgassed under dynamic vacuum

at 423 K for 6 h. The textural properties were determined from the adsorption/desorption isotherms by using the MicroActiveTristar II Plus software version 2.03. The BET surface area was determined using the multipoint BET algorithm in the P/P_0 range of 0.10–0.25. Average pore diameter (D_{pore}) was determined by the Barrett-Joyner-Halenda (BJH) equation on the desorption branch.

The Fourier transformed infrared spectra (FTIR) were recorded over the 4000–400 cm^{-1} range on a Thermo Scientific Nicolet iS50 FTIR spectrometer. Morphological properties and related punctual atomic composition of the samples were observed by transmission electron microscopy (TEM Jeol 2100 plus operated at 200 kV and equipped with a LaB_6 crystal) and field-emission scanning electron microscopy (SEM-FEG Hitachi SU-70 equipped with an EDS microanalysis (EDAX Genesis)). X-ray Photoelectron Spectroscopy (XPS) was performed on a AXIS Ultra^{DLD} spectrometer (Kratos Analytical) with a monochromatic Al Kα X-ray source (1486.6 eV). High resolution spectra were collected with a constant pass energy (PE = 20 eV) and the binding energy was calibrated with the adventitious C1s (284.8 eV). Quantification and spectral decomposition were processed using CasaXPS software.

Temperature programmed reductions (TPR) were carried out on 60 mg of sample under 5 vol% H_2/Ar gas flow (50 mL/min) with a heating rate of 10 °C/min up to 1000 °C using a Micromeritics Autochem II 2920 apparatus. Stoichiometry of La and Mn in the solids and in the filtrates (following the acid washing process) were monitored by inductively coupled plasma-optical emission spectroscopy (ICP-OES) (Agilent Technologies 700 Series spectrometer). Before elemental analysis, the solids were dissolved in a concentrated HCl/HNO_3 mixture. O_2 temperature-programmed desorption experiments (TPD) coupled with mass spectrometry were performed on the solids in situ pre-activated under 5 vol% O_2 diluted in He. The catalysts (50 mg) were submitted to the following conditions: 30 mL/min He, temperature from 40 °C to 1000 °C with a ramp of 10 °C/min. The outlet gases O_2 (m/z = 32) were identified using a mass spectrometer. The amount of O_2 desorbed from the catalyst was quantified from calibrated pulses (1 μmol).

3. Results and discussion

3.1. Crystal phase structure

In order to link the perovskite structure dissolution with time under acid treatment, XRD patterns of $LaMnO_{3.15}$ (LMO) solids treated with different durations (from 10 min to 22 h) have been recorded. As depicted in Fig. 1, below 180 min of acid treatment all diffraction peaks can be indexed by a rhombohedral lattice of pure LMO perovskite (JCPDS No. 50-0298) [37]. This indicates that, up to 180 min, the native perovskite is structurally unchanged. The average crystallite size of native LMO and LMO treated for 10 min, 60 min, and 180 min present similar values of 25.4 nm, 25.1 nm, 24.6 nm and 27.4 nm respectively, according to the Scherrer equation applied to the (0 2 4) plane (2θ = 46.9°). The Scherrer equation is not applied to main (1 1 0) and (1 0 4) planes (2θ = 32.5° and 32.8°) because their resulting diffraction peaks were confounded into one large peak. From 240 min, a new diffraction peak arises at 2θ = 37.1°. This peak becomes more noticeable after 360 min. Interestingly, the average crystallite sizes of the LMO phase decreases to 17.8 nm and 17.1 nm after 240 min and 360 min, respectively. After 14 h, the perovskite phase completely disappears to the profit of a new crystalline phase. In the previous work of Si et al. [21], they reported that the acid etching of a 3D ordered macroporous (3DOM) LMO perovskite led to the formation of a γ-MnO_2 phase (JCPDS No. 14–0644). Herein, different features are clearly obtained when etching is performed under our conditions (Fig. S1). Albeit some diffraction peaks from the XRD patterns of LM-14h and LM-22h (2θ = 21.9°, 37.1°, 40.5°, and 56.0°) can be indexed by a γ-MnO_2 phase already found by Si et al., additional peaks characteristic of such phase are missing. In literature, De Wolff et al. suggested that the γ-MnO_2 structure was built from microscopic intergrowths of ramsdellite and pyrolusite (β-MnO_2) phases, forming an alternation of (1 × 2) and (1 × 1) tunnels [38,39]. One model was further proposed by Chabre and Pannetier [40], which allowed a successful correlation between structural features and surface properties. In this model, the degree of intergrowth (called the De Wolff disorder) could be quantified by the shift of the (1 2 0) line [40]. In addition, a second type of growth defect in the ramsdellite lattice, named microtwinning (Tw), was assumed and used to amend the (1 2 0) line shift [41]. According to the above model, the X-ray diffraction patterns of LM-14h and LM-22h exhibit only two broad and symmetrical reflexions in the range 54° < 2θ < 71° (see Fig. 1), which are comparable to the XRD patterns of manganese dioxide prepared electrochemically (EMDs) [18–20,42]. Additionally, the absence of the diffraction peak indexed (0 3 1) further indicates that LM-14h and LM-22h sample structures belong unambiguously to the ε-MnO_2 phase (JCPDS No. 30-0820) [40]. As highlighted in Fig. S1, all diffraction peaks in the sample LM-22h can be indexed by the ε-MnO_2 phase reference. The large shoulder above 2θ = 21.9° could be attributed to the presence of highly charged Mn^{4+} cations located in antiphase domain boundaries, causing a local lattice expansion by electrostatic repulsion [42]. Hence, we report here for the first time a ε-MnO_2 phase obtained from a pure LMO perovskite using a simple acid etching method.

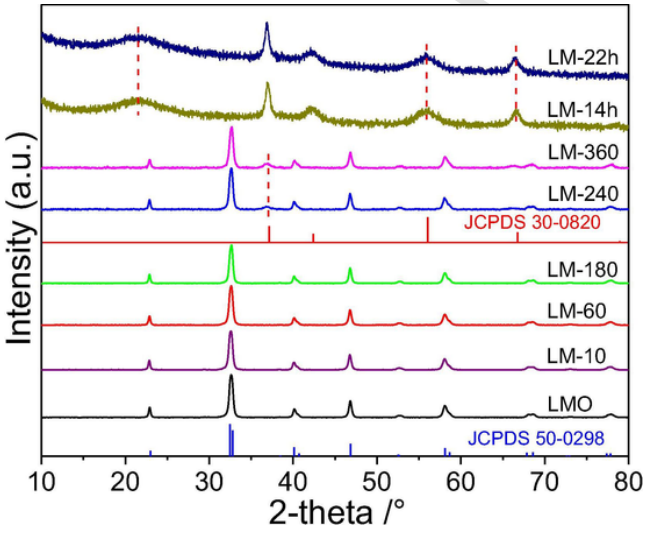

Fig. 1. Wide-angle XRD patterns of acid treated samples.

3.2. Textural properties

The N_2 adsorption/desorption isotherms and subsequent pore size distribution profiles of the solid series are presented in Fig. 2 (selected materials) and Fig. S2 (all synthetised materials). As depicted in Fig. 2, pure LMO exhibits a type II isotherm as highlighted by the mono-multilayer adsorption profile and the weak slope obtained in the BET linear domain, corroborating with the formation of a non porous-macroporous perovskite material. Derived LM-10, LM-60 and LM-180 acid treated samples display a similar isotherm profile with additional H4 or H3 hysteresis loop, revealing a type II-type IV composite isotherm with a weak adsorption step due to capillary condensation at relative pressures (P/P_0) ~ 0.5–0.9 and ~ 0.9–1.0, suggesting the formation of some mesoporosity within the samples (Figs. 2a and S2a). Progressive formation of a steep adsorption step accompanied with a large hysteresis loop is occuring in the materials LM-240 and LM-360 (Figs. 2a and S2a), with well-distributed pore diameters around 7 nm. In parallel, the lower average pore diameter determined on the desorp-

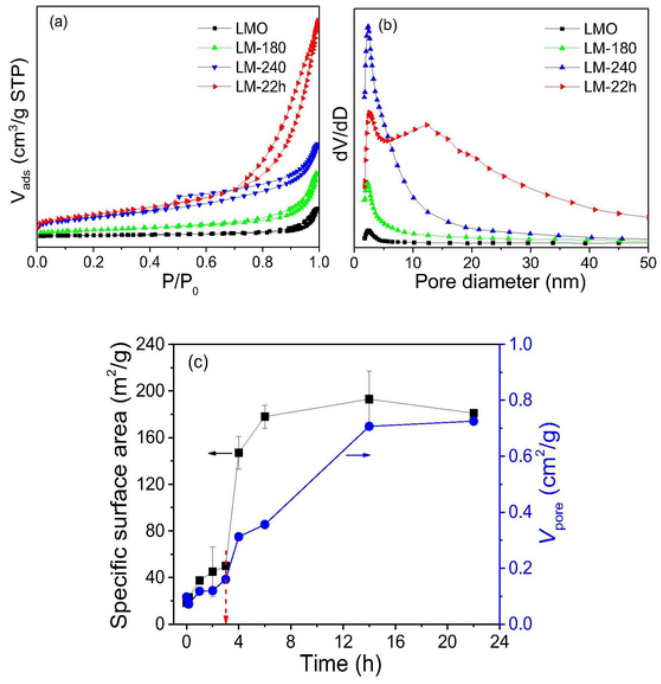

Fig. 2. (a) N_2 physisorption isotherms and (b) pore-size distributions of acid treated samples, (c) specific surface area and total pore volume changes upon reaction time of acid treatment (error bar estimated from two independent experiments).

tion branch and the twofold increase of the total pore volume (Table 1) all point toward the generation of small mesopores on LM-240 and LM-360. These latter features coincide with the presence of the first traces of ε-MnO_2 obtained by XRD, thus reasonably suggesting that the self-ordering of ε-MnO_2 nanocrystals leads to the formation of a tailored intercrystalline mesoporosity. From 14 h of acid treatment, it can be noticed that the obtained ε-MnO_2 materials (LM-14h and LM-22h) display a predominant type IV isotherm with H3 hysteresis loop and a strong perturbation at high relative pressure with the absence of plateau, revealing the formation of a hierarchical meso/macro-porous ε-MnO_2 material (Figs. 2a and S2a). As shown in Figs. 2b and S2b, the pore diameter distribution becomes wider and moves toward larger pore sizes. To conclude, acid treatment led to the formation of intercrystalline mesoporosity due to the overtime formation, growth and further assembly of the ε-MnO_2 crystals.

To demonstrate the impact of the acid treatment on the resulting textural properties, the BET surface area and the total pore volume were correlated to the acid treatment duration in Fig. 2c. As expected, the surface area of pure LMO perovskite obtained by the conventional "citrate" complexation route is only 18 m^2/g, typical of native LMO perovskites [37]. The BET surface area of samples increased significantly upon acid treatment time (the related values are summarized in Table 1). Before 180 min, the BET surface area of the samples progressively increased and reached a value of 49 m^2/g with a total pore volume of 0.16 cm^3/g (Table 1). After 240 min, a sharp increase of the BET surface area is observed, from 49 m^2/g to 147 m^2/g, which is corroborated with the formation of ε-MnO_2 nanosheets as earlier indicated by the XRD patterns. Finally, extending the acid treatment time to 14 h and 22 h boosts the BET surface areas of the resulting ε-MnO_2 materials up to 180 m^2/g (Fig. 2c) with total pore volumes exceeding 0.70 cm^3/g (Table 1). Hence, we demonstrate a clear correlation between structural changes and textural properties of the materials. LMO physical properties can be modified, and controlled to some extent, by applying a judicious time of acid treatment.

Table 1
Textural and structural properties of native and acid treated LMO samples.

Sample	S_{BET}	Crystalline phase [a]	V_{pore}	D_{pore}
	(m^2/g)		(cm^3/g)	(nm)
LMO	18	LMO	0.10	21.8
LM-10	23	LMO	0.07	23.2
LM-60	37	LMO	0.12	11.1
LM-180	49	LMO	0.16	13.3
LM-240	147	LMO/ε-MnO_2	0.31	6.7
LM-360	178	LMO/ε-MnO_2	0.36	6.9
LM-14h	193	ε-MnO_2	0.71	13.8
LM-22h	181	ε-MnO_2	0.73	19.0

[a] As identified by X-ray diffraction.

3.3. Morphology (TEM and SEM)

Surface morphologies (including elemental analysis) of LMO perovskite particles and their acid-treated counterparts were directly visualized by TEM/EDS (Fig. 3) and SEM (Fig. 4) analyses. As shown in Fig. 3a, the native LMO perovskite is composed of agglomerated small particles with size ranging from 20 to 50 nm, that could form intercrystalline mesopores (Fig. S3a, b) in a macroporous network (Fig. S4a, b). The energy dispersive spectrometry (EDS01) (inset of Fig. 3a) indicated that these particles are La-enriched (Table S1) as typically observed on native perovskites [43]. From the high-resolution TEM (HRTEM) in Fig. 3b, d-spacing values of 0.28 nm and 0.39 nm can be indexed by the (1 1 0) and (0 1 2) planes ($d_{(1\,1\,0)}$ = 0.276 nm and $d_{(0\,1\,2)}$ = 0.386 nm) of native LMO (JCPDS file n° 50-0298). After 180 min of acid treatment, a mixture of two particle morphologies is observed: smooth and visible particles comparable to the initial perovskite particles, and filiform solids at their surface (Figs. 3c and S3c). This observation is coherent with the textural characterization, showing an overall increase of both BET surface area and total pore vol-

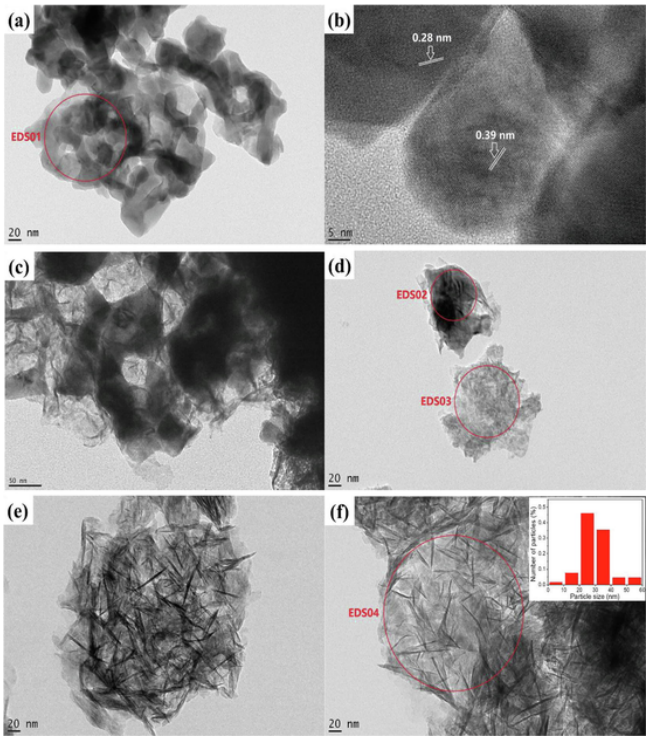

Fig. 3. TEM micrographs and EDS elemental mapping (insets) of (a and b) LMO, (c) LM-180, (d) LM-240, (e and f) LM-22h.

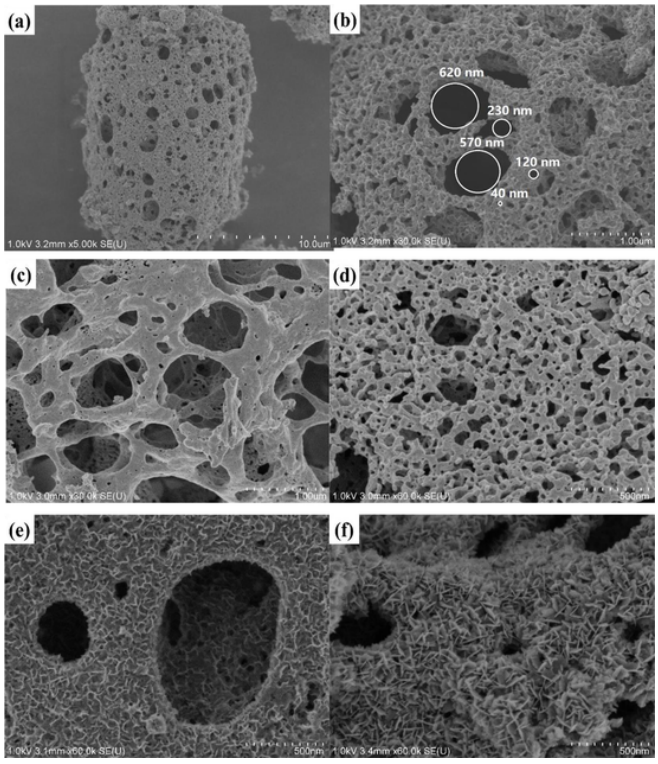

Fig. 4. SEM micrographs of (a and b) LM-180, (c-e) LM-240, (f) LM-22h.

ume. Between LM-180 and LM-240, few differences can be seen at low magnitude (Fig. 4a–d). Both samples are composed of macrostructures exhibiting a disordered yet interconnected meso/macro-porous network (Fig. 4a and c) and generally made of aggregated particles of LMO perovskite (Fig. 4b and d, Figs. S4c and S4d). However, their rough surface (Fig. 4a, b) was smoothened (Fig. 4c, d) under acid etching. Moreover, additional features can be further observed on several regions in LM-240, with their surface presenting a filiform morphology (Figs. 4e, S3d and S4e). Correlated to ε-MnO_2 detection by XRD, EDS (Fig. 3d) clearly demonstrates that the filiform morphology can be attributed to almost pure manganese oxide particles (EDS03, La/Mn = 0.04) (Table S1), while the dense particles present the elemental composition of native LMO perovskite (EDS02, La/Mn = 1.01) (Table S1). Finally, different lattice fringe distances can be measured by HRTEM on LM-240. In Fig. S3e, the presence of residual LMO perovskite phase ($d_{(1\,1\,0)}$ = 0.276 nm and $d_{(0\,1\,2)}$ = 0.386 nm) was confirmed. A *d*-spacing value of 0.40 nm is observed which can be indexed to (0 1 2) plane of native LMO (d_{LMO} (0 1 2) = 0.386 nm), or by a non-attributed plane of ε-MnO_2 (*d* = 0.42 nm, JCPDS PDF# 30–0820), or by the (1 0 1) plane of ramsdellite (*d*(1 0 1) = 0.405 nm, JCPDS PDF# 43–1455). Additionally, *d*-spacing value of 0.24 nm (Fig. S3f) can be indexed by the (1 0 0) plane of ε-MnO_2 ($d_{(1\,0\,0)}$ = 0.242 nm) [42]. These results confirm the formation of mixed macro/meso-porous LMO/ε-MnO_2 composite material (LM-240) as previously found by XRD analysis (Fig. 1).

After 22 h, LMO perovskite particles are completely converted into nanosheets of ε-MnO_2 (Figs. 3e, 4f, S4f) presenting a desert rose morphology. Those intergrown nanosheets present a length/width size comprised between 20 and 90 nm (average: 41 nm) (inserts in Figs. 3f and S3g) and an average thickness of 4 nm, as indicated by the measurement of 100 particles from TEM analysis (Image J Software). We attempt to estimate the crystallite size of LM-22h solid according to the Scherrer equation. Such equation was applied to the main peak obtained at 37°. The average crystallite size found for LM-22h presents a mean value of 18 nm which is lower with respect to TEM analysis (~41 nm). In our case, such discrepancies could arise from the low crystallinity of ε-MnO_2 particles as well as a filiform morphology which is not take into account in the Sherrer approximation (i.e. shape factor). The macrostructure still retains pores ranging from the mesopore to the macropore domains, which is coherent with N_2 physisorption isotherms. Sole ε-MnO_2 presence is comforted by HRTEM (Fig. S3h) where only one lattice fringe is observed with a *d*-spacing value of 0.24 nm, indexed by its (1 0 0) plane. Moreover, the EDS analysis (EDS04, insert in Fig. 3f) confirms that nanosheets are exempt from lanthanum (Table S1). Those datas are consistent with XRD and ICP elementary analysis results (Table 2). From these above considerations, the combination of TEM and SEM allowed us to visualize a morphological transformation happening during acid etching, from dense and aggregated particles of LMO perovskite to intergrown nanosheets of ε-MnO_2. Absence of lanthanum was confirmed by EDS in LM-22h. However, the large macrostructure seems barely affected by this conversion, advocating for a pseudomorphic transformation process which will be discussed after.

3.4. ICP and XPS analysis

Surface composition and surface chemical states were evaluated by X-ray photoelectron spectroscopy (XPS). The quantitative elemental compositions including atomic concentration of La $3d_{5/2}$ and Mn $2p_{3/2}$, and atomic ratio of La/Mn, Mn^{4+}/Mn^{3+} and O_{latt}/O_{ads} are summarized on Table 2. The N 1 s XPS peaks were also recorded and show similar, low trace of nitrogen species at the XPS limit detection in all samples (not shown here). First, the surface La/Mn atomic ratio as given by XPS for native LMO perovskite (La/Mn = 1.27) is higher than the bulk value (La/Mn = 1.00) obtained by ICP (Fig. 5a), which is comparable to the theoretical value of LMO perovskite (La/Mn = 1). This higher atomic ratio is in agreement with the reported A-site enrichment at the surface of native LMO perovskite. According to ICP and XPS (Table 2), both bulk and surface La/Mn atomic ratios decrease with increasing the acid treatment duration. Notably, the decreasing rate of La/Mn atomic ratio in the bulk (ICP) was slower than at the surface (XPS), which might indicate that the acid etching is an outside-inward process. This observation further supports a pseudomorphic transformation process.

Now, in order to investigate the dissolution process, we studied the cation concentrations within the acidic filtered liquor at various treatment times by ICP (Fig. 5b). As illustrated, La^{3+} species gradually increased and almost reached the maximal theoretical value after 360 min. This trend is consistent with XPS (Fig. S5), showing a gradual decrease of the La 3d peaks intensity. In contrast, the Mn^{2+} con-

Table 2
Relative surface abundances of the elements constituting the native and acid treated LMO samples.

Sample	La/Mn atomic ratio		La $3d_{5/2}$	Mn $2p_{3/2}$	Mn^{4+}/Mn^{3+}	O_{latt}/O_{ads}
	ICP	XPS	at%	at%		
LMO	1	1.27	21.7	17.1	0.28	2.47
LM-10	0.78	0.79	12.6	16	0.32	1.96
LM-60	0.7	0.65	13.9	21.5	0.72	3.13
LM-180	0.62	0.35	8.9	24.7	0.87	3.66
LM-240	0.17	0.12	3.5	29.3	1.09	3.91
LM-360	0.13	0.07	2	28.9	1.28	3.94
LM-14h	0	0.003	0.1	33.7	2	4.3
LM-22h	0	0.005	0.2	33	1.71	3.76

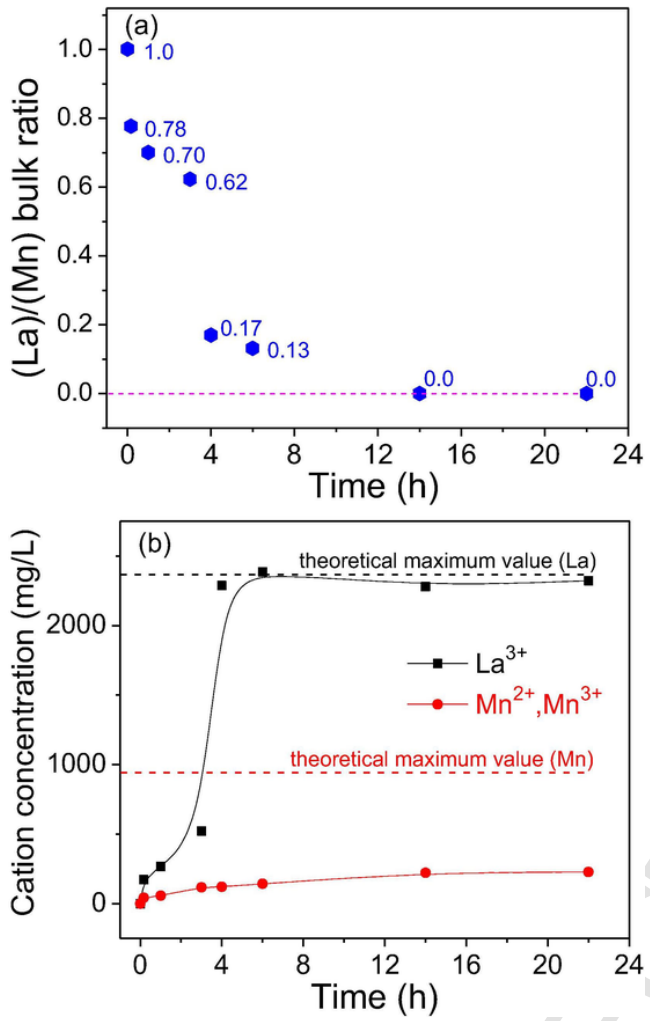

Fig. 5. Evolutions of (a) La/Mn cation ratio in bulk samples and (b) cations dissolution (La and Mn) upon reaction time according to the ICP analysis.

centration increased slowly and was nearly stable after 14 h, corresponding to a loss of about 25% of the Mn from the native LMO perovskite (Fig. 5b). These results directly confirm that the composition of the materials changes from La-rich to Mn-rich surface, with almost pure ε-MnO_2 materials obtained after 14 h.

XPS spectra in the Mn 2p region can be observed in Fig. 6. The asymetrical main Mn $2p_{3/2}$ peak shows the presence of both Mn^{3+} and Mn^{4+}, which present a multiplet splitting [44]. That is why the decomposition of Mn $2p_{3/2}$ was obtained based on reference spectra of Mn_2O_3 and MnO_2 powder samples with binding energies at 641.6 and 642.2 eV, respectively [45]. For the native LMO, the surface Mn^{4+}/Mn^{3+} atomic ratio is about 0.28. After acid treatment, as indicated in Table 2, the Mn^{4+}/Mn^{3+} atomic ratio increased gradually with the decreasing La/Mn atomic ratio. This result can be attributed to the dismutation reaction of dissolved Mn^{3+}, which will be discussed in the following part. This reaction seems to proceed slowly and the Mn^{4+}/Mn^{3+} atomic ratio reached 1.71 after 22 h of acid treatment (Table 2), confirming the increased presence of Mn^{4+} species which may also promote the stabilisation of surface oxygen vacancies [28]. In Fig. S6, the O1s photopic region of the LMO and LM-22h materials showed several contributions at positions P1 = 529.3, 530.0 eV; P2 = 530.9, 531.4 eV, and P3 = 532.0, 532.6 eV. P1, P2 and P3 were respectively assigned to the surface lattice oxygen (O^{2-}, denoted as O_{latt}), various surface adsorbed oxygen species (O_2^-, O_2^{2-}/O^- and hydroxyl/carbonate, denoted as O_{ads}), and physisorbed water on the surface [46,47]. The alteration of the LMO structure along with the enrichment of the solid with Mn species on the surface induce the shifting of the three peaks in the LM-22h sample toward a higher binding energy, with respect to the parent LMO. Additionally, the O_{latt}/O_{ads} molar ratio on catalyst surface increased from 2.47 (LMO) to 3.76 (LM-22h) while extending the acid etching time (Table 2). As discussed above, the progressive leaching of La^{3+} species along with the dismutation reaction of dissolved Mn^{3+} species result in an increased Mn^{4+}/Mn^{3+} ratio on the surface. The latter may induce more oxygen (O_{latt}) bonding to Mn^{4+} due to the physico-chemical transformation of the solid structure with a subsequent increase of O_{latt}/O_{ads} ratio. This is well in line with the decrease of the P2 contribution in LM-22h corresponding to surface oxygen species (see Fig. S6). Now, it has been reported that a combination of high Mn^{4+}/Mn^{3+} atomic ratio and high content of active lattice oxygen species on catalyst surfaces could lead to improved catalytic activity [15,48,49]. This phenomenon is also in good agreement with the observed catalytic activities and the H_2-TPR results in the following discussion.

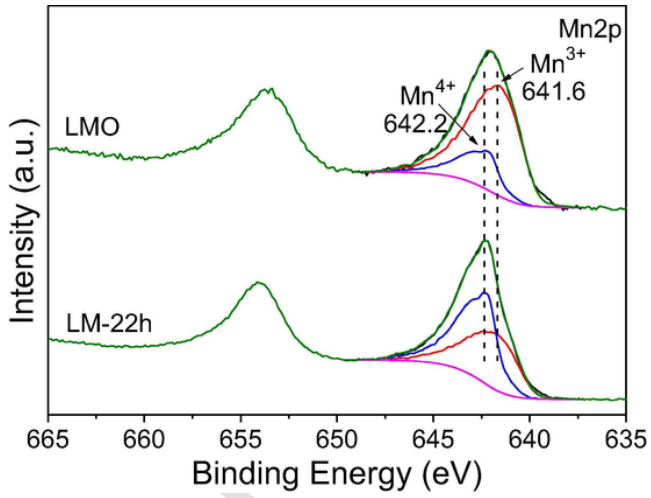

Fig. 6. Typical XPS spectra of Mn 2p of the acid treated samples: cases of LMO and LM-22h.

3.5. Tentative mechanism of perovskite conversion toward ε-MnO_2

Owing to the different characterization techniques used, we unveiled the conversion process of the native LMO perovskite toward the ε-MnO_2 phase in the presence of 3 M nitric acid. The La^{3+} species are completely dissolved from the perovskite structure, as proven by EDS (Fig. 3f), ICP (Fig. 5a, b) and XPS (Fig. S5). We also observe by ICP (Fig. 5b) a partial dissolution of the manganese species, up to 25% of the theoretical maximum value. Meanwhile, the Mn^{4+}/Mn^{3+} molar ratio gradually increased overtime within the solids (XPS, Table 2).

Regarding the literature, the acid digestion of Mn_2O_3 ores to produce ε-MnO_2 was extensively studied for batteries application. While Mn^{4+} presents a low solubility, and thus is likely to remain as MnO_6 building blocks, Mn^{3+} has a consequent solubility at room temperature and high acid concentration [39]. Moreover, under acidic conditions Mn^{3+} is highly sensitive to dismutation-precipitation reactions. Thus Mn^{3+} ions in solution would dismute into Mn^{2+} and Mn^{4+} following the overall reaction (1):

$$Mn_2O_3 + 2H^+ \leftrightarrow MnO_2 + Mn^{2+} + H_2O \quad (1)$$

This reaction is highly products-favoured, and explains both the presence of manganese in solution as Mn^{2+}, which is highly soluble, and the increase of the Mn^{4+}/Mn^{3+} molar ratio. Furthermore, as (1)

is highly products-favoured, we can assume that the mobility of the dissolved Mn^{3+} species during the process is low. This implies that Mn^{4+} ions are formed at the vicinity of the solid particles and precipitate back to assemble with the MnO_6 building blocks. The MnO_6 aggregations may grow in size by the continuous supply of MnO_6 units and in an oriented fashion, generating ε-MnO_2 nanosheets, while the presence of Mn^{3+} species generate microstructural defaults *via* the condensation of hydroxylated $[Mn(OH_2)_5(OH)]^{2+}$ species [39]. We assume that those microstructural defaults are responsible for the ε-MnO_2 structure [40]. Hence, if a LMO perovskite sample was soaked for a sufficient time under strong acidic conditions, pure ε-MnO_2 should be obtained.

Finally, as the macrostructure seems preserved and enlarged during the total conversion of LMO perovskite particles into ε-MnO_2 nanosheets (SEM, Fig. 4), a pseudomorphic transformation mechanism has been tentatively proposed as illustrated in Fig. 7. This mechanism, reported in the case of metal-organic frameworks [50], zeolites [51], and alumina [52], is based on a subtle equilibrium between dissolution and recrystallization kinetics which we clearly observed under our experimental conditions.

3.6. Reducibility and oxygen reactivity studies

Temperature programmed reduction (TPR) of H_2 was conducted to examine the reducibility of the material series characterized above, which should be closely related to their catalytic performance. The H_2-TPR profiles of the prepared samples are presented in Fig. 8 and Fig. S7, and their quantitative analysis data are listed in Table 3. For the native LMO, the first main peak is centered at 371 °C, with a shoulder at 430 °C which can be assigned to the reduction of Mn^{4+} to Mn^{3+} and the reduction of some Mn^{3+} located in a coordination-unsaturated microenvironment into Mn^{2+}, respectively [53,54]. Moreover, the weak peak at 270 °C is most likely due to the removal of over-stoichiometric oxygen accommodated within the lattice and oxygen adsorbed species (adspecies), which are weakly bounded [28,54,55]. The intense peak in the range of 600–900 °C corresponds to the reduction of the remaining Mn^{3+} to Mn^{2+}. Theoretically, if all of the manganese ions in LMO perovskite (Mn^{3+} and Mn^{4+}) were reduced to Mn^{2+}, the H_2 consumption of $LaMnO_{3.15}$ should be 2.70 mmol/g. As shown in Table 3, the calculated total H_2 consumption of the native LMO is 2.66 mmol/g, which is close to the theoretical value. During the initial step of acid treatment (10 to 180 min), the main peak at 371 °C shifts toward lower temperatures, which can be attributed to a facilitated reduction of Mn^{4+} owing to the formation of a meso/macro-porous network (Fig. 4) [54]. Meanwhile, the intensity of the peak at 270 °C increased gradually, which means that the acid treatment increases the total amount of oxygen species accommodated within the lattice. The peak at 430 °C fades away, which may be due to the loss by dissolution and/or dismutation of Mn^{3+}. In addition, the total H_2 consumption in the range of 200–500 °C increased gradually with a H_2-uptake of 1.56, 1.73, 1.90 and 1.93 mmol/g for samples LMO, LM-10, LM-60 and LM-180, respectively (Table 3). This is correlated to the increase of the Mn^{4+}/Mn^{3+} atomic ratio, as observed by XPS. Furthermore, the samples LM-240 and LM-360 exhibited similar TPR curves with only two reduction temperatures at 302/309 °C and 410 °C, which can be reasonably attributed to the two reduction steps of manganese oxide: $Mn^{4+} \rightarrow Mn^{3+}$ and $Mn^{3+} \rightarrow Mn^{2+}$ [21]. As shown by XRD, these two samples were mixtures of LMO perovskite and manganese oxide, which is supported here by observing a small peak at 783 °C with a H_2-uptake of 0.40 (LM-240) and 0.29 (LM-360) mmol/g. This peak is ascribed to the reduction of Mn^{3+} in acid-treated LMO phase, which appears earlier than that of native LMO (818 °C).

Finally, no reduction peak over 600 °C was observed in samples LM-14h and LM-22h, demonstrating the formation of pure MnO_2. The position of the main peak at 297 °C (LM-14h) and 294 °C (LM-22h) were the lowest among all samples, further suggesting that they present low-temperature reducibility and high oxygen mobility, which should have a positive effect over their catalytic performance for organic combustion. As calculated from the H_2-TPR profiles, by means of the acid treatment, the H_2 consumption at low temperature (200–500 °C), as well as the total H_2 consumption of materials increased gradually, and a drastic boost was found after 240 min of acid treatment (Table 3). This indicates that the average valence of Mn cations increased significantly, as proven by XPS data (Table 2).

In order to estimate the oxygen reactivity within the different solid structures, oxygen TPD profiles are showing the MS signal (m/z = 32) typically obtained for LMO, LM-240 and LM-22h (Fig. S8), since a similarity was observed for the reduction profiles of LM-240 and LM-22h at low temperature domains (Fig. 8). The profiles clearly show three O_2 desorption domains for all materials except for the parent LMO (Fig. S8a). The latter only exhibits one main region of oxygen loss with an onset desorption temperature > 800 °C, which is characteristic of the release of oxygen species from the solid bulk. Such results confirm the weak reactivity of surface oxygen species from LMO as no oxygen loss is observed at low temperature. Different features are observed on LM-240 composite with the occurrence of two desorption peaks at low temperature (T = 380 °C and 570 °C) which are in agree-

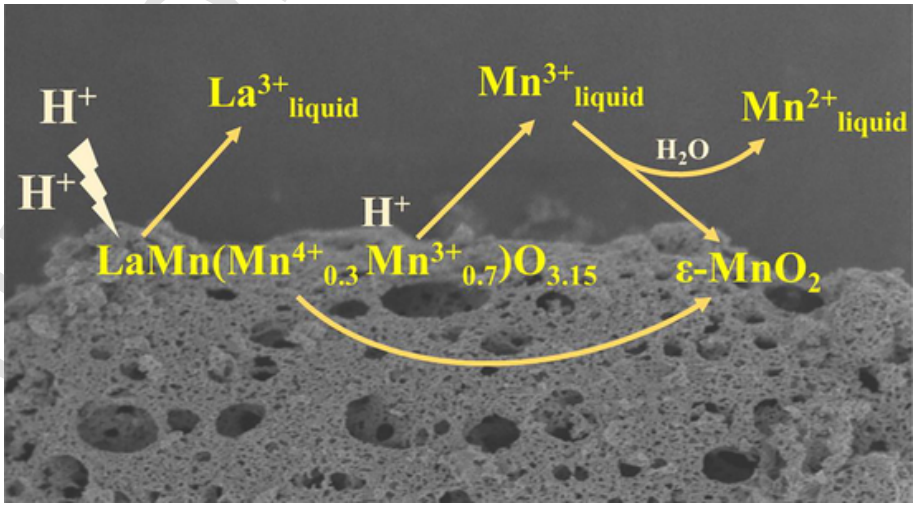

Fig. 7. Tentative mechanism of pseudomorphic transformation from LMO into ε-MnO_2.

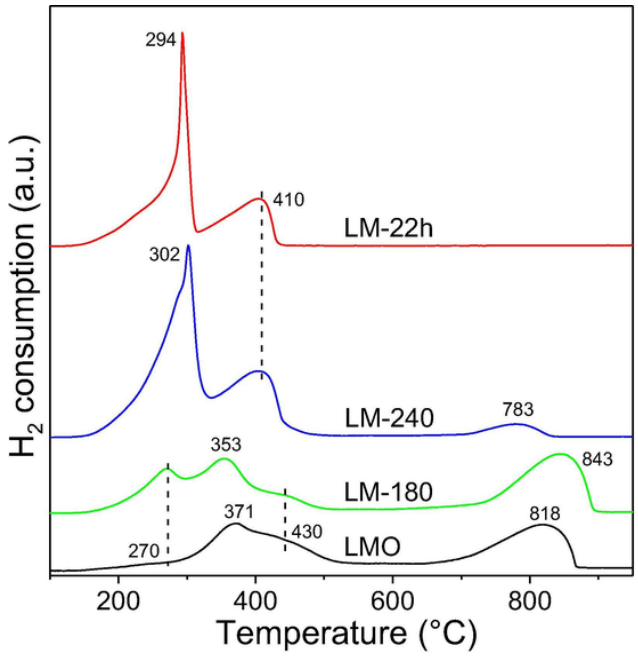

Fig. 8. H_2-TPR profiles of the acid treated samples.

Table 3
H_2 consumption deduced from the H_2-TPR for the native and acid treated LMO samples.

Sample	T reduction peaks (°C)		H_2 consumption (mmol/g)		
	Low T (200–500 °C)	High T (500–900 °C)	Low T (200–500 °C)	High T (500–900 °C)	Total
LMO	371	818	1.56	1.10	2.66
LM-10	354	816	1.73	1.07	2.80
LM-60	348	805	1.90	0.98	2.88
LM-180	354	843	1.93	1.19	3.12
LM-240	302	783	6.46	0.40	6.86
LM-360	309	783	6.76	0.29	7.05
LM-14h	297	–	8.98	–	8.98
LM-22h	294	–	7.99	–	7.99

ment with the loss of α and β oxygen species as described from previous works [56,57]. The first peak of LM-240 exhibits a clear shoulder below 400 °C that can result from desorption of surface oxygen species (e.g. O^- and O_2^-) and the release of labile oxygen species from the sub-surface lattice. The nature of the following desorptions at T = 380 °C and T = 570 °C could be linked to the diffusion of oxygen out of the lattice (partial reduction of manganese species). The ease of oxygen loss at low temperature can be reasonably explained by the surface enrichment of the solid by different Mn-bonded oxygen species. As a consequence, further surface enrichment obtained on LM-22h (Fig. S8b) is responsible of the increase of O_2 desorption at low temperature due to the presence of more adsorbed active surface oxygen (oxygen defects), and better accessibility of surface manganese species with respect to LMO-240 and LMO. Such results suggest that the acid treated LMO materials induce strong changes in the oxygen mobility but also in the concentration of surface active oxygen species. Taking into account the above bulk characterizations, a higher mobility and reactivity of surface oxygen species is observed for LM-22h with respect to its counterparts, and would further be helpful to boost the catalytic performance.

3.7. Catalytic activity

Formaldehyde (HCHO) oxidation was investigated for the LMO, LM-180, LM-240 and LM-22h (ε-MnO_2) materials. Fig. 9a shows the conversion efficiency of HCHO to CO_2 over the four catalysts with increasing temperature. The reaction temperatures of T10, T50, and T90 (corresponding to HCHO conversions of 10, 50, and 90% respectively) are summarized in Table 4. As expected, the catalytic performance

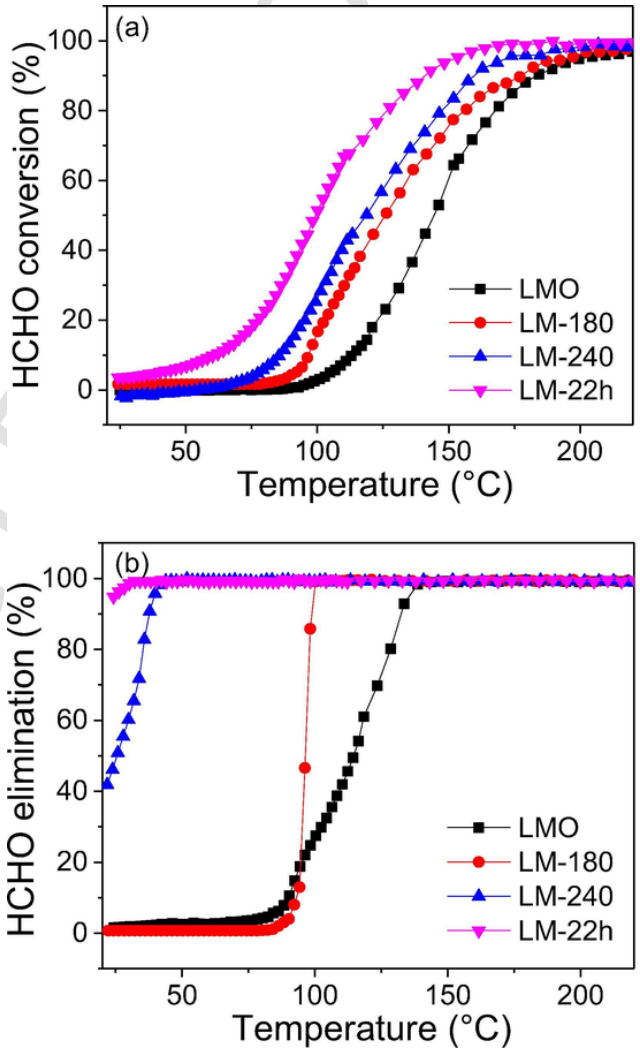

Fig. 9. Catalytic performance of HCHO over four selected samples: (a) HCHO conversion (into CO_2), (b) HCHO elimination.

Table 4
Catalytic activity of four selected materials for HCHO oxidation.

Sample	HCHO conversion temperature (°C)		
	T10	T50	T90
LMO	114	145	185
LM-180	97	126	177
LM-240	85	118	159
LM-22h	60	99	141

for HCHO oxidation using the acid treated samples (LM-180, LM-240 and LM-22h) were better than that of the native LMO.

As given in Table 4, the sample LM-22h corresponding to the hierarchical ε-MnO_2 catalyst achieved a T50 temperature of 99 °C, which is significantly lower with respect to LM-240 (118 °C), LM-180 (126 °C) and LMO (145 °C). Besides, the ε-MnO_2 phase produced in our work is showing one of the best T50 (99 °C) compared with other MnO_2 materials reported in literature (Table 5) with experimental conditions excluding the presence of water. Only the 3D ordered mesoporous MnO_2 catalyst, obtained from a sophisticated hard templating method [49], is showing a slightly lower T50 (90 °C) but with a HCHO concentration four times higher (Table 5). Additionally, as shown in Fig. 9b, the hierarchical ε-MnO_2 catalyst could totally eliminate, by adsorption, the HCHO at room temperature. As discussed above, ε-MnO_2 catalyst owned the largest BET surface area, as well as the highest surface Mn^{4+}/Mn^{3+} atomic ratio and O_{latt}/O_{ads} atomic ratio among all tested catalysts. Hence these advantages may be the reason why the hierarchical ε-MnO_2 catalyst possessed the highest catalytic activity in HCHO oxidation, while retaining excellent adsorption capacity at room temperature.

Table 5
Summary of MnO_2-based catalyst applied to catalytic oxidation of HCHO.

Catalyst	Reaction conditions	T50 (°C)	Ref.
ε-MnO_2	100 ppm of HCHO, GHSV: 30 L g_{cat}^{-1} h^{-1}, 20 vol% O_2, He balance	99	In this work
Pyrolusite (β-MnO_x with 1 × 1 tunnel)	400 ppm of HCHO, GHSV: 18000 h^{-1}, 10 vol% O_2, N_2 balance	150	[58]
Cryptomelane (α-MnO_x with 2 × 2 tunnel)		110	
Todorokite (3 × 3 tunnel)		140	
Cocoon-like MnO_2	460 ppm of HCHO, GHSV: 20 L g_{cat}^{-1} h^{-1}	130	[59]
Urchin-like MnO_2		120	
α-MnO_2	400 ppm of HCHO, GHSV: 30 L g_{cat}^{-1} h^{-1}, 21 vol% O_2, N_2 balance	150	[62]
β-MnO_2		100	
3D-MnO_2		90	
α-MnO_x	170 ppm of HCHO, GHSV: 100 L g_{cat}^{-1} h^{-1}, 20 vol% O_2, 25% Relative humidity, N_2 balance	~90	[49]
β-MnO_x		~140	
γ-MnO_x		~125	
δ-MnO_x		~60	
α-MnO_2-100	100 ppm of HCHO, GHSV: 90 L g_{cat}^{-1} h^{-1}, 21 vol% O_2, 70% Relative humidity, N_2 balance	125	[60]
α-MnO_2-110		100	
α-MnO_2-310		35	
Birnessite (V_{Mn}-1)	40 ppm of HCHO, GHSV: 120 L g_{cat}^{-1} h^{-1}, 21 vol% O_2, ~80% Relative humidity	84	[61]
Birnessite (V_{Mn}-2)		77	
Birnessite (V_{Mn}-3)		53	
Surface pits δ-MnO_2	200 ppm of HCHO, GHSV: 120 L g_{cat}^{-1} h^{-1}, 21 vol% O_2, ~45% Relative humidity	85	[63]
δ-MnO_2-P1		74	
δ-MnO_2-P2		62	

3.8. Mechanism of HCHO oxidation

To further investigate the mechanism of HCHO decomposition, infrared spectroscopic measurements (ATR-FTIR) were performed to observe if any changes occured on pure ε-MnO_2 external surface after HCHO exposure. Spectra were recorded before and after HCHO catalytic oxidation test and are presented in Fig. 10. Over the fresh catalyst, two bands at 1632 cm^{-1} and 3285 cm^{-1} ascribable to –OH groups (ν(OH) and δ(H_2O)) are observed. After HCHO oxidation, four new bands appeared: two at 1354 and 1572 cm^{-1}, belonging to the formate species ν_s(COO) and ν_{as}(COO) respectively; and two at 1387 and 2837 cm^{-1}, ascribed to hydrocarbonates δ(CH) and ν(CH) respectively [10,64]. As previously reported in literature [61,65], these results indicate that the oxidation of HCHO generate formate species, which may further react with surface oxygen species to form hydrocarbonates. Moreover, the decrease of ν(OH) and δ(H_2O) intensities might suggest that the formation of carbonate and formate species consumed the superficial –OH groups. It has been reported that superficial –OH groups play an important role during HCHO oxidation since they enhance the adsorption of HCHO *via* hydrogen bonding, especially at low temperature [64]. The XPS C1s peaks of the sample before and after HCHO conversion were used to explore the formation of surface intermediates (Fig. 12d). Three peaks at 284.8 eV, 286.3 eV and 288.6 eV can be ascribable to sp^3-hybridized C (adventitious carbon), C-OH groups and carbonate (CO_3^{2-}) respectively. After the catalytic test, a new component at 288.3 eV belonging to the carboxylic C species (O═C–O) was observed, further confirming the formate formation during HCHO oxidation [64,65].

Our experimental results underline that HCHO oxidation on pure ε-MnO_2 is likely to follow the pathway: HCOO-M + OH-M → CO_2 + H_2O + 2 M (where M = Mn surface site). That is, the formate species ($HCOO^-_{ads}$) will first be generated due to the reaction of the adsorbed HCHO with surface active oxygen (O_{latt}, O_2^-, O^-, or superficial –OH groups). At high temperature, the formate species will be further oxidized into CO_2 owing the successive participation of these oxygen species. This is in line with the literature [10,61,64–66]. Moreover, the mole of water formed per mole of oxydized formaldehyde could regenerate the surface active oxygen, allowing to explain the long-term activity observed even in dry conditions (see thereafter). Herein, the outstanding catalytic activity of the hierarchical ε-MnO_2

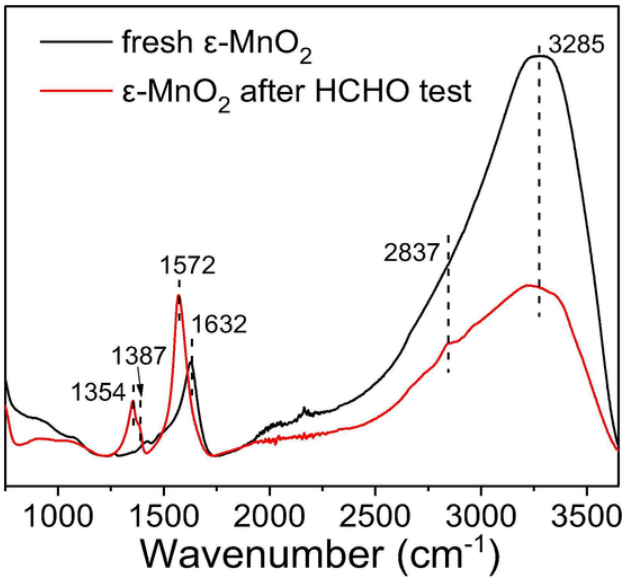

Fig. 10. ATR-FTIR spectra of sample LM-22h (ε-MnO_2) before and after catalytic test.

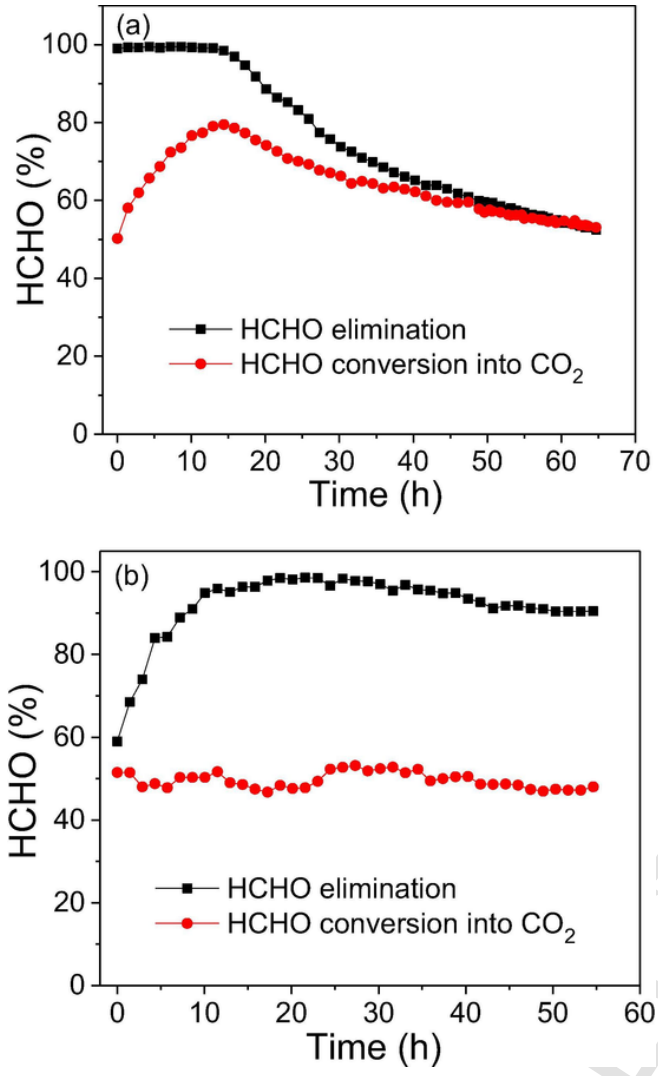

Fig. 11. (a) HCHO conversion with time on stream over LM-22h (ε-MnO_2), (b) Effect of moisture on HCHO conversion with time on stream over LM-22h (T = 99 °C).

catalyst may be due to the cumulative effect of several factors. On one hand, ε-MnO_2 presents a meso/macro-porous skeleton and a large BET surface area, maximizing the diffusion of HCHO within the catalyst and supplying more external active sites. Furthermore, more superficial –OH groups increase the adsorption capacity of HCHO. The chemisorption of HCHO at the surface of a catalyst is always the crucial step to trigger its oxidation [64]. On the other hand, a good oxygen mobility, the high oxidizing ability and the abundance of active oxygen species at the surface of ε-MnO_2 could further enhance its catalytic performance. The migration of oxygen species and oxygen activation are dependent on the redox cycle of Mn^{4+}/Mn^{3+}. The enrichment in Mn^{4+} may enhance the redox cycles of ε-MnO_2, which is favorable for the oxidation of HCHO.

3.9. Stability test and moisture effect

From a practical point of view, stability issues of the catalysts should be taken into account. Fig. 11a illustrates the HCHO conversion over time on stream at 99 °C (corresponding to HCHO conversion of 50%) over ε-MnO_2, which achieved an exemplary long-term stability after 65 h. Interestingly, during the initial stage (0 ~ 12 h) an enhancement of HCHO conversion is observed. After 12 h, a continuous decrease of both the HCHO elimination and HCHO conversion into CO_2

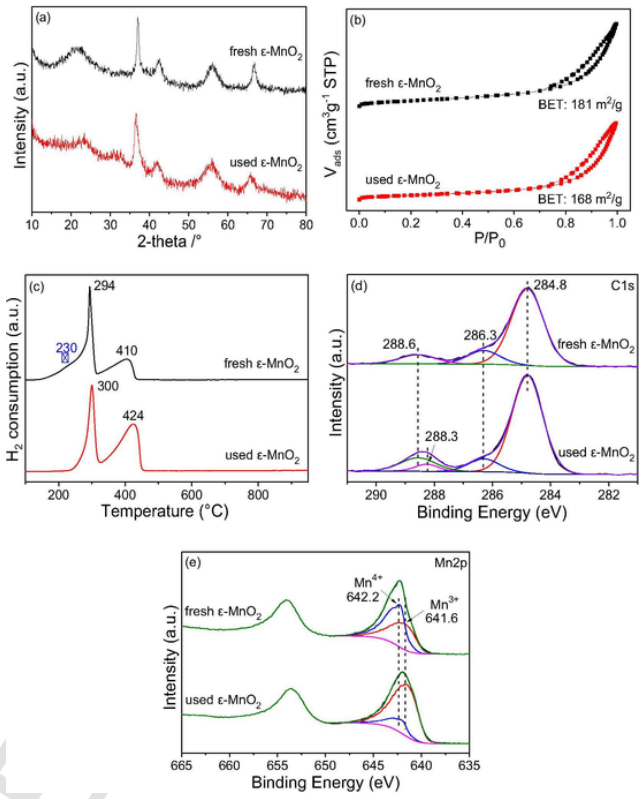

Fig. 12. Characterization of (a) XRD, (b) BET,(c) TPR, (d) XPS spectra of C1s, (e) XPS spectra of Mn2p for sample LM-22h (ε-MnO_2) before and after HCHO stability test.

was measured, indicating that during the initial stage HCHO was partly adsorbed until saturation. We speculate that the HCHO adsorbed on the catalyst from the beginning might interact with more HCHO molecules *via* hydrogen bonding in a similar manner than the superficial –OH groups or water and further enhance the conversion of HCHO. In addition, some highly active and non-renewable adsorbed oxygen species on the catalyst surface might be also involved in HCHO oxidation in the beginning. While the HCHO conversion decreased gradually after 12 h at T50, stabilization occurred from 65 h, with comparable values obtained for HCHO elimination and HCHO conversion into CO_2. At this stage, the catalyst worked under stationnary conditions (no simultaneous storage and selective conversion to CO_2).

The used ε-MnO_2 catalyst was further characterized by XRD, BET, XPS and TPR. As indicated in Fig. 12a and b, no appreciable changes of its textural or structural properties were observed compared to the as-made ε-MnO_2. Additionally, the H_2-TPR profile (Fig. 12c) of the used ε-MnO_2 exhibited small shifts to higher temperatures, indicating that its reducibility was slightly lower. Also, the amount of consumed H_2 was lower for the used sample (5.98 mmol/g) compared to the fresh one (7.99 mmol/g), implying that more Mn species with lower valence state are present in the used catalyst after HCHO oxidation. Moreover, the relative area ratio of the low (around 300 °C) to the high-temperature (around 424 °C) reductions was lower for the used sample in comparison with that of the fresh one (Fig. 12c), indicating a decreased Mn^{4+}/Mn^{3+} ratio after the stability test. Of note, a peak around 230 °C (see the blue star) disappeared in H_2-TPR profile of the used ε-MnO_2, demonstrating the consumption of non-renewable surface oxygen species during the HCHO oxidation. The evolution of Mn^{4+}/Mn^{3+} molar ratios over the sample before and after HCHO oxidation were further compared (Fig. 12e). After HCHO oxidation, Mn^{4+}/Mn^{3+} surface atomic ratio decreased from 1.71 to 0.26, decreasing the average oxidation state (AOS) of the surface Mn from 3.63 to 3.21. Such results indicate that the valence of the used ε-MnO_2 leans toward a + 3 oxida-

tion state, which is in good agreement with the H_2-TPR analysis. These results relate greatly with the oxidation of HCHO into formate species with the probable consumption of surface active oxygen, including lattice oxygen (O_{latt}), resulting in global manganese oxide reduction, without alteration of the global catalyst activity.

Moisture is a key factor in the catalytic oxidation of HCHO, which seems to have a dual role as either a promoting or an inhibiting effect on the conversion of HCHO. It has been reported that moisture is one of the major reasons causing a negative effect on catalytic activity through its competitive adsorption on active sites [48]. Conversely, previous works found that moisture could act as a promoter that enhance the catalytic oxidation of HCHO (See T50 values of Table 5), as it not only facilitates the regeneration of superficial –OH groups but it is also beneficial to the desorption of carbonate *via* competitive adsorption [64,67]. Thus, the effect of moisture on the conversion of HCHO was investigated by adding water to the inlet gas (corresponding to a relative moisture capacity of 46% at room temperature). As shown in Fig. 11b, the presence of water has no negative or positive effect on the material activity, with only a slight decrease of the HCHO conversion (-2%) measured after at least 55 h. Moreover, the catalytic stability seems improved over time. This could be due to the regeneration of surface active oxygen species, as previously reported [64,67]. In order to elucidate this point, O_2-TPD studies with the MS signal (m/z = 32) were performed for LM-22h (ε-MnO_2) before and after test. As described before, three O_2 desorption domains were observed in Fig. S8. Two desorption peaks at low temperature (T = 450 °C and 545 °C) are corresponding to the loss of α and β oxygen species, while the last region of oxygen loss (T > 800 °C) is characteristic of the release of oxygen species from the solid bulk. Of note, the quantity of O_2 released from ε-MnO_2 after HCHO oxidation seems to be slightly higher compared with that of fresh ε-MnO_2 (Fig. S8a), especially for the O_2 desorption domain linking to the diffusion of oxygen out of the lattice. As calculated in Fig. S8b, the used ε-MnO_2 possesses nearly equivalent (a bit less) content of surface oxygen species (Peak 1 and Peak 2) but more bulk oxygen species (Peak 3) with respect to the fresh ε-MnO_2. Such results confirmed that surface active oxygen species could be regenerated during the HCHO oxidation in the presence of water. In addition, the presence of water strongly improved the capacity of adsorption of the catalyst since HCHO abatement was still maintained above 90% after 65 h test.

4. Conclusions

In this work, we report a simple and straightforward method adapted from a soft chemical process to prepare for the first time hierarchical porous ε-MnO_2 catalysts derived from a pure $LaMnO_{3.15}$ perovskite. Complementary experiments used in this study demonstrate that the complete dissolution of La^{3+} cations could occur in the presence of 3 M HNO_3 while preserving the macroporous skeleton of the native perovskite. Moreover, direct link is given between material's properties (i.e. BET surface areas, total pore volumes, structural phase changes) and the acid treatment time applied. More specifically, XPS and H_2-TPR analyses revealed higher concentration of Mn^{4+} active species present in the acid-treated material compared to the native LMO perovskite. At the light of the results, a pseudomorphic transformation is proposed to occur *via* a dissolution/recrystallization process involving dismuted Mn species, leading to the formation of a meso/macro-porous macrostructure composed of intergrown nanosheets of ε-MnO_2. The hierarchical porous ε-MnO_2 was found to be stable and highly-efficient for low-temperature catalytic oxidation of HCHO, owing to an increase of its BET surface area and an improvement of its redox properties. In addition, excellent stability of the pure ε-MnO_2 catalyst in the presence of water was still observed after 50 h test (50% selective conversion of HCHO at T = 99 °C), confirming the potential of these materials for indoor depollution processes.

Acknowledgments

The authors thank the Chevreul Institute (FR 2638) for its help in the development of this work. Chevreul Institute is supported by the « Ministère de l'Enseignement Supérieur et de la Recherche », the « Région Nord-Pas de calais » and the « Fonds Européen de Développement des Régions ». Yin XU thanks the China Scholarship Council (No. 201606270079) for the financial support for the PhD program. Authors acknowledge Dr. Sandra Casale (Université Pierre et Marie Curie, Paris VII, France) and Olivier Gardoll (Université de Lille, UCCS UMR CNRS 8181, France) for conducting respectively electron microscopy (SEM-FEG HITACHI SU-70 and TEM 2100 plus) and O2-TPD on the materials.

Declaration of Competing Interest

None.

Appendix A. Supplementary data

Supplementary data to this article can be found online at https://doi.org/10.1016/j.cej.2020.124146.

References

[1] T. Salthammer, S. Mentese, R. Marutzky, Formaldehyde in the indoor environment, Chem. Rev. 110 (2010) 2536–2572.
[2] J.J. Collins, R. Ness, R.W. Tyl, N. Krivanek, N.A. Esmen, T.A. Hall, A review of adverse pregnancy outcomes and formaldehyde exposure in human and animal studies, Regul. Toxicol. Pharm. 34 (2001) 17–34.
[3] ARC.IARC classifies formaldehye as carcinogenic to humans; press release no.153; International Agency for Research on Cancer: Lyon, 2004.
[4] X. Feng, H. Liu, C. He, Z. Shen, T. Wang, Synergistic effects and mechanism of a non-thermal plasma catalysis system in volatile organic compound removal: a review, Catal. Sci. Technol. 8 (2018) 936–954.
[5] S.P. Rong, P.Y. Zhang, J.L. Wang, F. Liu, Y.J. Yang, G.L. Yang, S. Liu, Ultrathin manganese dioxide nanosheets for formaldehyde removal and regeneration performance, Chem. Eng. J. 306 (2016) 1172–1179.
[6] J.P. Bellat, I. Bezverkhyy, G. Weber, S. Royer, R. Averlant, J.M. Giraudon, J.F. Lamonier, Capture of formaldehyde by adsorption on nanoporous materials, J. Hazard. Mater. 300 (2015) 711–717.
[7] X. Zhu, D.L. Chang, X.S. Li, Z.G. Sun, X.Q. Deng, A.M. Zhu, Inherent rate constants and humidity impact factors of anatase TiO_2 film in photocatalytic removal of formaldehyde from air, Chem. Eng. J. 279 (2015) 897–903.
[8] X.B. Zhu, C. Jin, X.S. Li, J.L. Liu, Z.G. Sun, C. Shi, X.G. Li, A.M. Zhu, Photocatalytic formaldehyde oxidation over plasmonic Au/TiO_2 under visible light: moisture indispensability and light enhancement, ACS Catal. 7 (2017) 6514–6524.
[9] S. Royer, D. Duprez, F. Can, X. Courtois, C.B. Dupeyrat, S. Laassiri, H. Alamdari, Perovskites as substitutes of noble metals for heterogeneous catalysis: dream or reality, Chem. Rev. 114 (2014) 10292–10368.
[10] J. Quiroz, J.M. Giraudon, A. Gervasini, C. Dujardin, C. Lancelot, M. Trentesaux, J.F. Lamonier, Total oxidation of formaldehyde over MnO_x-CeO_2 catalysts: the effect of acid treatment, ACS Catal. 5 (2015) 2260–2269.
[11] C. Ciotonea, R. Averlant, G. Rochard, A.S. Mamede, J.M. Giraudon, H. Alamdari, J.F. Lamonier, S. Royer, A simple and green procedure to prepare efficient manganese oxide nanopowder for the low temperature removal of formaldehyde, ChemCatChem 9 (2017) 2366–2376.
[12] Y. Wang, C.J. Jiang, Y. Le, B. Cheng, J.G. Yu, Hierarchical honeycomb-like Pt/NiFe-LDH/rGO nanocomposite with excellent formaldehyde decomposition activity, Chem. Eng. J. 365 (2019) 378–388.
[13] J.Q. Torres, S. Royer, J.P. Bellat, J.M. Giraudon, J.F. Lamonier, Formaldehyde: catalytic oxidation as a promising soft way of elimination, ChemSusChem 6 (2013) 578–592.
[14] D. Sun, S. Wageh, A.A. Al-Ghamdi, Y. Le, J. Yu, C. Jiang, Pt/C@MnO_2 composite hierarchical hollow microspheres for catalytic formaldehyde decomposition at room temperature, Appl. Surf. Sci. 466 (2019) 301–308.
[15] J. Chen, D.X. Yan, Z. Xu, X. Chen, W.J. Xu, H.P. Jia, J. Chen, A novel redox precipitation to synthesize Au-doped α-MnO_2 with high dispersion toward low-temperature oxidation of formaldehyde, Environ. Sci. Technol. 52 (2018) 4728–4737.
[16] Y.L. Luo, J.C. Zuo, X.S. Feng, Q.R. Qian, Y.B. Zheng, D.F. Lin, B.Q. Huang, Q.H. Chen, Good interaction between well dispersed Pt and $LaCoO_3$ nanorods achieved rapid Co^{3+}/Co^{2+} redox cycle for total propane oxidation, Chem. Eng. J. 357 (2019) 395–403.
[17] Y. Wang, H. Arandiyan, J. Scott, A. Bagheri, H.X. Dai, R. Amal, Recent advances in ordered meso/macroporous metal oxides for heterogeneous catalysis: a review, J. Mater. Chem. A 5 (2017) 8825–8846.

[18] X.F. Hu, F.Y. Cheng, X.P. Han, T.R. Zhang, J. Chen, Oxygen bubble-templated hierarchical porous ε-MnO_2 as a superior catalyst for rechargeable Li-O_2 batteries, Small 11 (2015) 809–813.

[19] H. Chen, Y. Wang, Y.K. Lv, Catalytic oxidation of NO over MnO_2 with different crystal structures, RSC Adv. 6 (2016) 54032–54040.

[20] S.H. Kim, B.C. Park, Y.S. Jeon, Y.K. Kim, MnO_2 Nanowire-CeO_2 nanoparticle composite catalysts for the selective catalytic reduction of NOx with NH_3, ACS Appl. Mater. Interfaces 10 (2018) 32112–32119.

[21] W.Z. Si, Y. Wang, Y. Peng, J.H. Li, Selective dissolution of A-site Cations in ABO_3 perovskites: a new path to high-performance catalysts, Angew. Chem. Int. Ed. 127 (2015) 8065–8068.

[22] W.Z. Si, Y. Wang, Y. Peng, X. Li, K.Z. Li, J.H. Li, A high-efficiency γ-MnO_2-like catalyst in toluene combustion, Chem. Commun. 51 (2015) 14977–14980.

[23] W.Z. Si, Y. Wang, S. Zhao, F.Y. Hu, J.H. Li, A facile method for in situ preparation of the MnO_2/$LaMnO_3$ catalyst for the removal of toluene, Environ. Sci. Technol. 50 (2016) 4572–4578.

[24] J. Erlebacher, M.J. Aziz, A. Karma, N. Dimitrov, K. Sieradzki, Evolution of nanoporosity in dealloying, Nature 410 (2001) 450–453.

[25] M. Kudo, H. Ohkawa, W. Sugimoto, N. Kumada, Z. Liu, O. Terasaki, Y. Sugahara, A layered tungstic acid $H_2W_2O_7$ nH_2O with a double-octahedral sheet structure: conversion process from an aurivillius phase $Bi_2W_2O_9$ and structural characterization, Inorg. Chem. 42 (2003) 4479–4484.

[26] J. Gopalakrishnan, Chimie douce approaches to the synthesis of metastable oxide materials, Chem. Mater. 7 (1995) 1265–1275.

[27] W. Sugimoto, M. Shirata, Y. Sugahara, K. Kuroda, New conversion reaction of an aurivillius phase into the protonated form of the layered perovskite by the selective leaching of the bismuth oxide sheet, J. Am. Chem. Soc. 121 (1999) 11601–11602.

[28] K. Huang, X.F. Chu, L. Yuan, W.C. Feng, X.F. Wu, X.Y. Wang, S.H. Feng, Engineering the surface of perovskite $La_{0.5}Sr_{0.5}MnO_3$ for catalytic activity of CO oxidation, Chem. Commun. 50 (2014) 9200–9203.

[29] Y.H. Wei, L. Ni, M.X. Li, J.L. Zhao, A template-free method for preparation of MnO_2 catalysts with high surface areas, Catal. Today 297 (2017) 188–192.

[30] Y. Ding, S. Wang, L. Zhang, L.P. Chen, M.Z. Wang, S.D. Wang, A facile method to promote $LaMnO_3$ perovskite catalyst for combustion of methane, Catal. Commun. 97 (2017) 88–92.

[31] D. Wang, Y. Peng, Q. Yang, S.C. Xiong, J.H. Li, J. Crittenden, Performance of modified $La_xSr_{1-x}MnO_3$ perovskite catalysts for NH_3 oxidation: TPD, DFT, and kinetic studies, Environ. Sci. Technol. 52 (2018) 7443–7449.

[32] H.Z. Geng, K.K. Kim, K.P. So, Y.S. Lee, Y. Chang, Y.H. Lee, Effect of acid treatment on carbon nanotube-based flexible transparent conducting films, J. Am. Chem. Soc. 129 (2007) 7758–7759.

[33] A.H. Janssen, A.J. Koster, K.P. de Jong, Three-dimensional transmission electron microscopic observations of mesopores in dealuminated zeolite Y, Angew. Chem. Int. Ed. 40 (2001) 1102–1104.

[34] A. Schön, J.P. Dacquin, P. Granger, C. Dujardin, Non stoichiometric $La_{1-y}FeO_3$ perovskite-based catalysts as alternative to commercial three-way-catalysts?–Impact of Cu and Rh doping, Appl. Catal. B 223 (2018) 167–176.

[35] A. Schön, C. Dujardin, J.P. Dacquin, P. Granger, Enhancing catalytic activity of perovskite-based catalysts in three-way catalysis by surface composition optimisation, Catal. Today 258 (2015) 543–548.

[36] J. Faye, A. Baylet, M. Trentesaux, S. Royer, F. Dumeignil, D. Duprez, J.M. Tatibouët, Influence of lanthanum stoichiometry in $La_{1-x}FeO_{3-\delta}$ perovskites on their structure and catalytic performance in CH_4 total oxidation, Appl. Catal. B 126 (2012) 134–143.

[37] G. Kéranguéven, S. Royer, E. Savinova, Synthesis of efficient Vulcan-$LaMnO_3$ perovskite nanocomposite for the oxygen reduction reaction, Electrochem. Commun. 50 (2015) 28–31.

[38] P.M. De Wolff, Interpretation of some γ-MnO_2 diffraction patterns, Acta Crystallogr. 12 (1959) 341–345.

[39] D.K. Walanda, G.A. Lawrance, S.W. Donne, Kinetics of Mn_2O_3 digestion in H_2SO_4 solutions, J. Solid State Chem. 182 (2009) 1336–1342.

[40] Y. Chabre, J. Pannetier, Structural and electrochemical properties of the proton/γ-MnO_2 system, Prog. Solid State Chem. 23 (1995) 1–130.

[41] C.A. Dias, H. Santana, M.A.L. Nobre, M.C. Lopes, The relation between structural features and electrochemical activity of MnO_2 nanoparticles synthesized from a polyol-made Mn_3O_4 precursor, J. Solid State Electrochem. 17 (2013) 1967–1976.

[42] C.H. Kim, Z. Akase, L.C. Zhang, A.H. Heuer, A.E. Newman, P.J. Hughes, The structure and ordering of ε-MnO_2, J. Solid State Chem. 179 (2006) 753–774.

[43] D. Neagu, G. Tsekouras, D.N. Miller, H. Menard, J.T.S. Irvine, In situ growth of nanoparticles through control of non-stoichiometry, Nat. Chem. 5 (2013) 916–923.

[44] M.C. Biesinger, B.P. Payne, A.P. Grosvenor, L.W.M. Lau, A.R. Gerson, R.S.C. Smart, Resolving surface chemical states in XPS analysis of first row transition metals, oxides and hydroxides: Cr, Mn, Fe, Co and Ni, Appl. Surf. Sci. 257 (2011) 2717–2730.

[45] E. Symianakis, D. Malko, E. Ahmad, A.S. Mamede, J.F. Paul, N. Harrison, A. Kucernak, Electrochemical characterization and quantified surface termination obtained by low energy ion scattering and X-ray photoelectron spectroscopy of orthorhombic and rhombohedral $LaMnO_3$ powders, J. Phys. Chem. C 119 (2015) 12209–12217.

[46] V.P. Santos, M.F.R. Pereira, J.J.M. Órfão, J.L. Figueiredo, The role of lattice oxygen on the activity of manganese oxides towards the oxidation of volatile organic compounds, Appl. Catal. B 99 (2010) 353–363.

[47] N.A. Merino, B.P. Barbero, P. Eloy, L.E. Cadús, $La_{1-x}Ca_xCoO_3$ perovskite-type oxides: identification of the surface oxygen species by XPS, Appl. Surf. Sci. 253 (2006) 1489–1493.

[48] X.F. Tang, Y.G. Li, X.M. Huang, Y. Xu, H.Q. Zhu, J.G. Wang, W.J. Shen, MnO_x-CeO_2 mixed oxide catalysts for complete oxidation of formaldehyde: effect of preparation method and calcination temperature, Appl. Catal. B 62 (2006) 265–273.

[49] J. Zhang, Y. Li, L. Wang, C. Zhang, H. He, Catalytic oxidation of formaldehyde over manganese oxides with different crystal structures, Catal. Sci. Technol. 5 (2015) 2305–2313.

[50] J. Reboul, S. Furukawa, N. Horike, M. Tsotsalas, K. Hirai, H. Uehara, M. Kondo, N. Louvain, O. Sakata, S. Kitagawa, Mesoscopic architectures of porous coordination polymers fabricated by pseudomorphic replication, Nat. Mater. 11 (2012) 717–723.

[51] M. Choi, K. Na, R. Ryoo, The synthesis of a hierarchically porous BEA zeolite via pseudomorphic crystallization, Chem. Commun. 20 (2009) 2845–2847.

[52] H. De Souza Santons, P.K. Kiyohara, P. De Souza Santos, Pseudomorphic transformations of euhedral crystals of γ-AlOOH into aluminas, Ceram. Int. 20 (1994) 175–181.

[53] S. Royer, H. Alamdari, D. Duprez, S. Kaliaguine, Oxygen storage capacity of $La_{1-x}A'_xBO_3$ perovskites (with A′ = Sr, Ce; B = Co, Mn)-relation with catalytic activity in the CH_4 oxidation reaction, Appl. Catal. B 58 (2005) 273–288.

[54] Y.X. Liu, H.X. Dai, Y.C. Du, J.G. Deng, L. Zhang, Z.X. Zhao, Lysine-aided PMMA-templating preparation and high performance of three-dimensionally ordered macroporous $LaMnO_3$ with mesoporous walls for the catalytic combustion of toluene, Appl. Catal. B 119 (2012) 20–31.

[55] Y.J. Zhu, Y.Q. Sun, X.Y. Niu, F.L. Yuan, H.G. Fu, Preparation of La-Mn-O perovskite catalyst by microwave irradiation method and its application to methane combustion, Catal. Lett. 135 (2010) 152–158.

[56] S. Royer, F. Berube, S. Kaliaguine, Effect of the synthesis conditions on the redox and catalytic properties in oxidation reactions of $LaCo_{1-x}Fe_xO_3$, Appl. Catal. A-Gen 282 (2005) 273–284.

[57] H. Najjar, J.F. Lamonier, O. Mentré, J.M. Giraudon, H. Batis, Optimization of the combustion synthesis towards efficient $LaMnO_{3+y}$ catalysts in methane oxidation, Appl. Catal. B 106 (2011) 149–159.

[58] T. Chen, H. Dou, X. Li, X. Tang, J. Li, J. Hao, Tunnel structure effect of manganese oxides in complete oxidation of formaldehyde, Micropor. Mesopor. Mater. 122 (2009) 270–274.

[59] X. Yu, J. He, D. Wang, Y. Hu, H. Tian, Z. He, Facile controlled synthesis of Pt/MnO_2 nanostructured catalysts and their catalytic performance for oxidative decomposition of formaldehyde, J. Phys. Chem. C 116 (2011) 851–860.

[60] S. Rong, P. Zhang, F. Liu, Y. Yang, Engineering crystal facet of α-MnO_2 nanowire for highly efficient catalytic oxidation of carcinogenic airborne formaldehyde, ACS Catal. 8 (2018) 3435–3446.

[61] J. Wang, J. Li, C. Jiang, P. Zhou, P. Zhang, J. Yu, The effect of manganese vacancy in birnessite-type MnO_2 on room-temperature oxidation of formaldehyde in air, Appl. Catal. B 204 (2017) 147–155.

[62] B. Bai, Q. Qiao, J. Li, J. Hao, Synthesis of three-dimensional ordered mesoporous MnO_2 and its catalytic performance in formaldehyde oxidation, Chin. J. Catal. 37 (2016) 27–31.

[63] J. Wang, G. Zhang, P. Zhang, Layered birnessite-type MnO_2 with surface pits for enhanced catalytic formaldehyde oxidation activity, J. Mater. Chem. A 5 (2017) 5719–5725.

[64] J.L. Wang, P.Y. Zhang, J.G. Li, C.J. Jiang, R. Yunus, J. Kim, Room-temperature oxidation of formaldehyde by layered manganese oxide: effect of water, Environ. Sci. Technol. 49 (2015) 12372–12379.

[65] S. Selvakumar, N. Nuns, M. Trentesaux, V.S. Batra, J.M. Giraudon, J.F. Lamonier, Reaction of formaldehyde over birnessite catalyst: a combined XPS and ToF-SIMS study, Appl. Catal. B 223 (2018) 192–200.

[66] C.B. Zhang, F.D. Liu, Y.P. Zhai, H. Ariga, N. Yi, Y.C. Liu, K. Asakura, M.F. Stephanopoulos, H. He, Alkali-metal-promoted Pt/TiO_2 opens a more efficient pathway to formaldehyde oxidation at ambient temperatures, Angew. Chem. Int. Ed. 51 (2012) 9628–9632.

[67] D.W. Kwon, P.W. Seo, G.J. Kim, S.C. Hong, Characteristics of the HCHO oxidation reaction over Pt/TiO_2 catalysts at room temperature: the effect of relative humidity on catalytic activity, Appl. Catal. B 163 (2015) 436–443.